

PAPER • OPEN ACCESS

## Magnetic targeting to enhance microbubble delivery in an occluded microarterial bifurcation

To cite this article: M de Saint Victor *et al* 2017 *Phys. Med. Biol.* **62** 7451

View the [article online](#) for updates and enhancements.

### Related content

- [Passive acoustic mapping of magnetic microbubbles for cavitation enhancement and localization](#)
- [Understanding the dynamics of superparamagnetic particles under the influence of high field gradient arrays](#)
- [In vitro thrombolytic efficacy of echogenic liposomes loaded with tissue plasminogen activator and octafluoropropane gas](#)

### Recent citations

- [A review of magnet systems for targeted drug delivery](#)  
Ya-Li Liu *et al*
- [Sonothrombolysis with Magnetically Targeted Microbubbles](#)  
Marie de Saint Victor *et al*
- [Comparing Strategies for Magnetic Functionalization of Microbubbles](#)  
Estelle Beguin *et al*



MR Safe  
4D Phantom  
for MRgRT

QUASAR<sup>MRI 4D</sup>  
BY MODUS CA

LEARN MORE ▶

# Magnetic targeting to enhance microbubble delivery in an occluded microarterial bifurcation

M de Saint Victor<sup>1</sup>, D Carugo<sup>1,2</sup>, L C Barnsley<sup>1,3</sup> , J Owen<sup>1</sup>, C-C Coussios<sup>1</sup> and E Stride<sup>1,4</sup> 

<sup>1</sup> Department of Engineering Science, Institute of Biomedical Engineering, University of Oxford, Oxford OX3 7DQ, United Kingdom

<sup>2</sup> Faculty of Engineering and the Environment, Mechatronics and Bioengineering Science Research Groups, University of Southampton, Southampton SO17 1BJ, United Kingdom

E-mail: [eleonor.stride@eng.ox.ac.uk](mailto:eleonor.stride@eng.ox.ac.uk)

Received 16 March 2017, revised 25 July 2017

Accepted for publication 10 August 2017

Published 5 September 2017



CrossMark

## Abstract

Ultrasound and microbubbles have been shown to accelerate the breakdown of blood clots both *in vitro* and *in vivo*. Clinical translation of this technology is still limited, however, in part by inefficient microbubble delivery to the thrombus. This study examines the obstacles to delivery posed by fluid dynamic conditions in occluded vasculature and investigates whether magnetic targeting can improve microbubble delivery. A 2D computational fluid dynamic model of a fully occluded Y-shaped microarterial bifurcation was developed to determine: (i) the fluid dynamic field in the vessel with inlet velocities from 1–100 mm s<sup>-1</sup> (corresponding to Reynolds numbers 0.25–25); (ii) the transport dynamics of fibrinolytic drugs; and (iii) the flow behavior of microbubbles with diameters in the clinically-relevant range (0.6–5 μm). *In vitro* experiments were carried out in a custom-built microfluidic device. The flow field was characterized using tracer particles, and fibrinolytic drug transport was assessed using fluorescence microscopy. Lipid-shelled magnetic microbubbles were fluorescently labelled to determine their spatial distribution within the microvascular model. In both the simulations and experiments,



Original content from this work may be used under the terms of the [Creative Commons Attribution 3.0 licence](https://creativecommons.org/licenses/by/3.0/). Any further distribution of this work must maintain attribution to the author(s) and the title of the work, journal citation and DOI.

<sup>3</sup> Present address: Jülich Centre for Neutron Science (JCNS) at Heinz Maier-Leibnitz Zentrum (MLZ), Forschungszentrum Jülich GmbH, Lichtenbergstrasse 1, D-85748 Garching, Germany.

<sup>4</sup> Author to whom any correspondence should be addressed.

the formation of laminar vortices and an abrupt reduction of fluid velocity were observed in the occluded branch of the bifurcation, severely limiting drug transport towards the occlusion. In the absence of a magnetic field, no microbubbles reached the occlusion, remaining trapped in the first vortex, within 350  $\mu\text{m}$  from the bifurcation center. The number of microbubbles trapped within the vortex decreased as the inlet velocity increased, but was independent of microbubble size. Application of a magnetic field (magnetic flux density of 76 mT, magnetic flux density gradient of  $10.90 \text{ T m}^{-1}$  at the centre of the bifurcation) enabled delivery of microbubbles to the occlusion and the number of microbubbles delivered increased with bubble size and with decreasing inlet velocity.

Keywords: magnetic targeting, thrombolysis, microbubbles, ultrasound, drug delivery

 Supplementary material for this article is available [online](#)

(Some figures may appear in colour only in the online journal)

## 1. Introduction

Despite therapeutic advances, ischemic stroke remains a leading cause of disability and mortality worldwide (Truelsén 2001, Feigin *et al* 2003). At present, intravenous tissue-plasminogen activator (tPA) is the only thrombolytic treatment approved by the U.S. Food and Drug Administration. However, due to its potentially severe side effects, it is subject to drastic exclusion criteria (The National Institute of Neurological Disorders and Stroke rt-PA Stroke Study Group 1995; American College of Emergency Physicians and American Academy of Neurology 2013) and only a fraction of the patient population is eligible for treatment (California Acute Stroke Pilot Registry Investigators 2005). Ultrasound and injected microbubble agents have emerged as a promising adjuvant treatment to increase the safety and efficacy of thrombolytic drugs, by improving the recanalization of occluded arteries (Alexandrov *et al* 2008, Perren *et al* 2008, Molina *et al* 2009), and possibly allowing a reduction in administered drug doses (Brown *et al* 2011, Petit *et al* 2012). Unfortunately, sonothrombolysis and conventional tPA therapy are both limited by inefficient agent delivery to the clot. Disrupted circulation of drug molecules to and around the clot has been identified as one of the primary causes of failure in pharmacological treatment of myocardial infarctions (Anderson 1997). For microbubble-based therapies, a marked depletion in microbubbles is also often observed in the ischemic region (Rezkalla and Kloner 2002, Kern *et al* 2011). As microbubble concentration in the thrombus area affects clot mass loss, this can affect therapeutic outcomes (Borrelli *et al* 2012). Culp *et al* highlighted the distinctive importance of microbubble delivery for *in vivo* thrombolysis using albumin microbubbles and low frequency ultrasound in canine arteriovenous grafts (Culp *et al* 2001). Complete recanalization was achieved in all animals that received direct microbubble injections into the occluded grafts (8/8), and only in 4 out of 10 that were treated with a systemic, intravenous injection (Culp *et al* 2001). Despite these reports, previous studies of drug and microbubble delivery in obstructed vasculature are very limited.

This study investigates the effect of magnetic targeting on microbubble delivery in thrombosed vessels. Magnetic targeting employs an externally applied magnetic field to control the location of magnetically responsive therapeutic agents *in vivo*. Recent work has shown the potential of this targeting method in non-occluded vascular networks, demonstrating

the feasibility of steering magnetic carriers into a specific branch of a Y-shaped bifurcation (Cherry and Eaton 2014, Tehrani *et al* 2015). Yet, to the best of the authors' knowledge, delivery of magnetically targeted particles has not been investigated in fully occluded vascular networks. In this study, it is hypothesized that an inexpensive permanent magnet system can aid microbubble steering through a vascular network towards an occluded blood vessel, and that this has the potential to enhance microbubble delivery for sonothrombolysis in the clinic. Suitable magnetic vehicles have already been developed. For instance, Torno *et al* have produced drug-loaded magnetic polymer microparticles and shown that, in conjunction with ultrasound, they accelerate recanalization in a single, straight vessel (Torno *et al* 2008). Owen *et al* have loaded lipid-coated microbubbles with iron oxide nanoparticles and shown that they can be retained with a magnet against clinically relevant flow conditions and at tissue depths of a few centimetres (Owen *et al* 2015).

The first objective of the present study was to investigate the influence of fluid velocity and microbubble physical properties upon the concentration of microbubbles in the occluded branch of a bifurcating vessel. The second objective was to evaluate the effect of magnetic targeting on magnetically responsive microbubbles in occluded vasculature, and to identify the physical parameters that affect the concentration of microbubbles successfully delivered to the occlusion. This was carried out using both computational fluid dynamic simulations and a physical microfluidic model of an occluded arteriolar bifurcation.

## 2. Materials and methods

### 2.1. Model geometries of complete microvascular occlusions

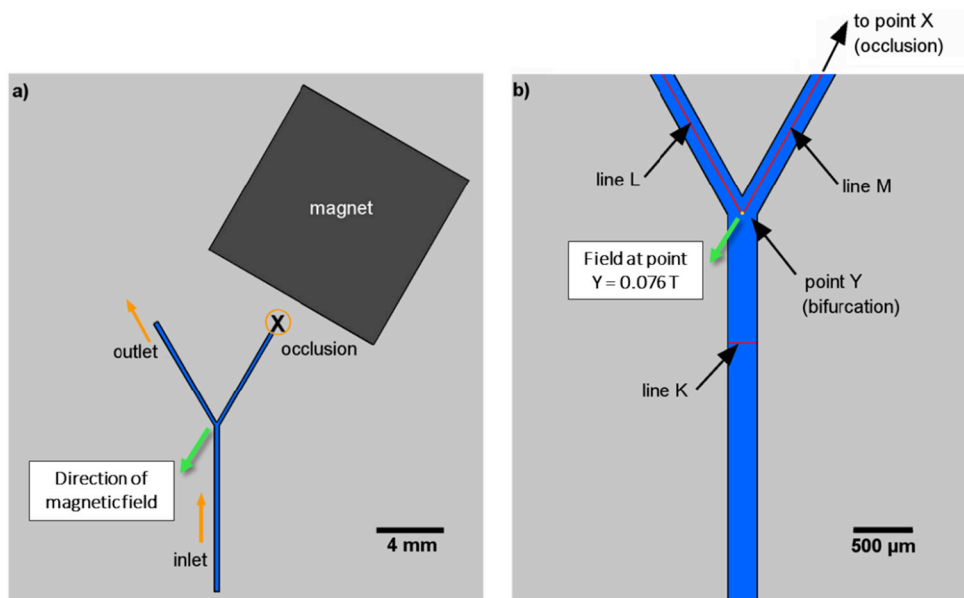
The simple case of a rigid, Y-shaped arteriolar bifurcation was considered, in which one of the daughter branches is fully occluded. Arteriolar occlusions caused by blood clots are recognised as a clinically relevant condition, and several studies have been conducted in order to investigate their physical and biological development, both experimentally (Matuskova 2006, Ni 2000, 2003) and computationally (Belyaev 2015, Fogelson 2015). Matuskova and co-authors investigated the effect of fibronectin plasmatic concentration on the dynamics of thrombotic and haemostatic processes in arterioles, using a mice model (Matuskova 2006). The arteriolar diameter was in the range 160–200  $\mu\text{m}$ . Ni *et al* investigated the role of different ligands on thrombus growth, in mice arterioles with a diameter in the range 80–120  $\mu\text{m}$  (Ni 2000). The same group investigated thrombus-induced, complete occlusion of mice arterioles (diameter 100–130  $\mu\text{m}$ ) associated with reduction in von Willebrand factor and fibrinogen. In a recent study, Jain *et al* developed a microfluidic device mimicking stenosed arteriolar vessels, to evaluate clot formation under pathophysiological flow regimes (Jain 2016). The arteriolar diameter in their model reduced from  $\sim 275$  to 125  $\mu\text{m}$ . In our study, the width of the parent branch was based on *in vivo* arteriolar diameters (Fung 1997), and is coherent with previous *in vivo* and *in vitro* studies investigating blood clot formation and progression in arterioles (Ni 2000, Matuskova 2006, Jain 2016). In addition, a complete arteriolar occlusion was replicated in our model, as this type of occlusion constitutes the majority of ST-elevation myocardial infarction cases (Chesebro *et al* 1987).

Table 1 and figure 1(a) summarize the geometry of the system. The central axis of the daughter branches formed a  $60^\circ$  angle with each other, which is comparable to the one of the *in vivo* arteriolar bifurcation architecture reported by Matuskova *et al* (2006). Their diameter was selected according to Murray's law, which predicts daughter branch size in a biological vessel network by computing minimal energy expenditure (Sherman 1981).

The inlet fluid velocity and the distance from the bifurcation position (point Y on figure 1(b)) to the occlusion (point X) were variable. The inlet velocities were within the range

**Table 1.** Dimensions of the micro arteriolar bifurcation model used in the numerical simulations and the *in vitro* experiments. The dimensions of the experimental bifurcation were adjusted to fit with the microfabrication constraints (i.e. size of the closest available milling tools).

Simulations (2D)	
Parent branch	Width $w_p = 250 \mu\text{m}$ . Length $l_p = 11 \text{ mm}$ .
Free daughter branch	Width $w_f = 180 \mu\text{m}$ . Length $l_f = 8 \text{ mm}$ .
Occluded daughter branch	Width $w_o = 180 \mu\text{m}$ . Length $l_o = (2-8) \text{ mm}$ .
Angle between daughter branches	$\alpha = 60^\circ$
Experiments (3D)	
Parent branch	Width $w_p = 250 \mu\text{m}$ . Depth $d_p = 200 \mu\text{m}$ . Length $l_p = 10 \text{ mm}$ .
Free daughter branch	Width $w_f = 178 \mu\text{m}$ . Depth $d_f = 200 \mu\text{m}$ . Length $l_f = 8 \text{ mm}$ .
Occluded daughter branch	Width $w_o = 178 \mu\text{m}$ . Depth $d_o = 200 \mu\text{m}$ . Length $l_o = 8 \text{ mm}$ .
Angle between daughter branches	$\alpha = 60^\circ$



**Figure 1.** Geometry of the microarterial system: (a) layout of the bifurcation; (b) lines and points of interest for analysis. The system consists of a rigid, Y-shaped bifurcation with a fully occluded branch, and a permanent magnet (NdFeB), placed 10 mm away from the center of the bifurcation. The magnitude of the magnetic field at point Y of the bifurcation is 0.076 T.

of physiologically relevant flow rates for vessels of this size, from  $1$  to  $100 \text{ mm s}^{-1}$  (corresponding to a Reynolds number in the range 0.25–25) (Fung 1997). The occluded branch length (distance X-Y) ranged from 2 to 8 mm, which is within the range of clinically observed lengths for such vessels (Fung 1997). To aid in the investigation, three lines of interest were

defined (figure 1(b)). Line K is perpendicular to the parent branch centerline and is located 1 mm before the bifurcation. Line L runs from the center of the bifurcation along the centerline of the unoccluded branch. Line M is symmetrical to line L in the occluded branch. The permanent magnet is represented by a half-inch square element, placed as shown in figure 1(a), with its magnetization vector parallel to line M and its surface 10 mm from the center of the bifurcation (point Y).

## 2.2. Numerical model

The numerical model was developed using COMSOL Multiphysics 5.0 software (COMSOL Ltd, Cambridge, UK) and employed to simulate: (i) fluid dynamic and magnetic fields in the steady-state; (ii) tissue plasminogen activator (tPA) concentration in the first hour after a bolus injection; and (iii) microbubble distribution in the first 150 s after a bolus injection. Table 2 contains the values that were chosen for the model parameters and physical constants.

**2.2.1. Discretization of the physical domain.** The physical domain under investigation was discretized into finite elements for numerical solving of the governing equations. It comprises two distinct regions: the space inside the channel (fine triangular mesh elements), and the space outside the channel (coarser triangular mesh elements). Further mesh refinement was applied at the edges of the channel, using a boundary layer meshing scheme. In each region, element size was chosen to be much smaller than the characteristic length of variation for the fluid velocity field and/or the magnetic field. The properties of the mesh are described in the supplementary data section (table S1) ([stacks.iop.org/PMB/62/7451/mmedia](http://stacks.iop.org/PMB/62/7451/mmedia)). A mesh independence study (figure S1) was carried out to determine the maximum allowable element size providing an accurate numerical solution.

**2.2.2. Hydrodynamic field.** With the geometry and mean inlet velocities described above, the Reynolds number in the parent channel of the bifurcation is:

$$\text{Re} = \frac{\rho u \Phi}{\eta}, \quad (1)$$

where  $\rho$  is the density of water,  $u$  is the mean inlet velocity,  $\Phi$  is the hydraulic diameter of the parent channel, and  $\eta$  is the dynamic viscosity of water. Re ranges from 0.25 to 25, clearly indicating that the flow is in a laminar regime.

The following mass conservation (continuity) and momentum conservation equations for incompressible flow were solved in the steady-state over the computational domain using COMSOL<sup>®</sup> and the ‘Laminar Flow’ interface of the ‘Computational Fluid Dynamic Module’:

$$\nabla \cdot (\rho \mathbf{u}) = 0 \quad (2)$$

and

$$\rho (\mathbf{u} \cdot \nabla) \mathbf{u} = -\nabla p \mathbf{I} + \nabla \cdot \left[ \eta (\nabla \mathbf{u} + \nabla \mathbf{u}^T) - \frac{2}{3} (\nabla \cdot \mathbf{u}) \mathbf{I} \right]. \quad (3)$$

At the channel walls, a no slip boundary condition was imposed. Past the bifurcation, the right-hand daughter branch was fully occluded (solid wall, no slip boundary condition at the occlusion), while the left-hand branch was the outlet (atmospheric pressure boundary condition at the extremity). The estimated entrance length of the parent branch,

$$L_e = 0.05 \text{Re} \Phi, \quad (4)$$

**Table 2.** Values of the parameters and physical constants used in the numerical model.

Parameter/constant	Name	Value
Density of air	$\rho_a$	$1.2754 \text{ kg m}^{-3}$
Density of water	$\rho$	$1000 \text{ kg m}^{-3}$
Dynamic viscosity of water	$\eta$	$8.9 \times 10^{-4} \text{ Pa} \cdot \text{s}$
Permeability of vacuum	$\mu_0$	$4\pi \times 10^{-7} \text{ H m}^{-1}$
Relative permittivity of the medium (water)	$\mu_m$	1
Remanent magnetization of NdFeB <sup>a</sup>	$M_{\text{NdFeB}}$	$1.14 \times 10^6 \text{ A m}^{-1}$
Saturation magnetization of particles	$M_s$	$4.7 \times 10^5 \text{ A m}^{-1}$ (Chikazumi 1997)
Diffusion coefficient of tPA <sup>b</sup>	$D_c$	$6 \times 10^{-11} \text{ m}^2 \text{ s}^{-1}$ (Young <i>et al</i> 1980, Torno <i>et al</i> 2008)
Correction factor	$\Gamma$	0.706
Volumetric ratio of particles in ferro fluid	$\beta_f$	0.1
Microbubble shell thickness	$R_s$	$5 \times 10^{-8} \text{ m}$

<sup>a</sup>Value provided by the manufacturer.

<sup>b</sup>Approximated with values from the literature for bovine serum albumin, a globular protein of similar molecular weight to tPA.

was  $275 \mu\text{m}$ . The microbubbles were therefore injected along line K, where the flow is fully developed.

**2.2.3. Magnetic field.** The magnetic flux density  $\mathbf{B}$  and the magnetic field intensity  $\mathbf{H}$  are linked by the material equation:

$$\mathbf{B} = \mu_0 (\mathbf{H} + \mathbf{M}), \quad (5)$$

where  $\mu_0$  is the magnetic permeability of vacuum and  $\mathbf{M}$  is the magnetization vector. The magnetic scalar potential  $V_m$  is defined as:

$$\mathbf{H} = -\nabla V_m \quad (6)$$

The Laplace equation:

$$\nabla^2 V_m = 0 \quad (7)$$

was solved for  $V_m$  using the ‘Magnetostatics, No Currents’ interface of the ‘AC/DC Module’ in COMSOL<sup>®</sup>. The following boundary conditions were applied: the normal component of  $\mathbf{B}$  is continuous at the surface of the magnet and vanishes at the perimeter of the simulation domain.

In the experimental set-up, the bifurcation was coplanar with the base of the magnet, but in the 2D simulation, it was assumed that the magnet geometry extends symmetrically above and below the simulation plane. To account for this difference, the simulated field  $\mathbf{B}$  inside the bifurcation was rescaled using a correction factor,  $\phi$ , so that the field at the bifurcation point of interest (point Y in figure 1(b)) agreed with the field predicted for the experimental geometry by a previously published 3D model (Barnsley *et al* 2015).

**2.2.4. Drug delivery.** Two factors contributed to drug transport through the bifurcation: drug advection with fluid flow and drug diffusion following the drug concentration gradient, described by Fick’s law. In addition, there were no chemical reactions in the system. Drug mass conservation therefore yields:

$$\frac{\partial c_d}{\partial t} + \nabla \cdot (-D_c \nabla c_d + c_d \mathbf{u}) = 0 \quad (8)$$

where  $c_d$  is the drug concentration,  $\mathbf{u}$  is the fluid velocity vector, and  $D_c$  is the diffusion coefficient for tPA in water at 20 °C.

tPA transport dynamics were computed in COMSOL<sup>®</sup> using the ‘Transport of diluted species’ interface of the ‘Chemical Species Transport’ module. The model was setup as a time-dependent study in time steps of 60 s over the course of an hour, a clinically relevant timeframe for stroke therapy (Hacke *et al* 2008). A constant, physiologically relevant concentration ( $6.2 \times 10^2 \text{ mol l}^{-1}$ ) of tPA was injected throughout treatment. Prior to drug injection at the fluid inlet, there was no drug in the bifurcation and the flow in the channel had reached a steady state.

**2.2.5. Microbubble delivery.** Each microbubble is subjected to a drag force  $\mathbf{F}_d$  from the fluid and to a magnetophoretic force  $\mathbf{F}_m$  from the magnetic field. Moreover, particles suspended in fluid flows may be subjected to inertial lift forces depending on the Reynolds number of the carrier fluid and the relative dimension of the particle with respect to the channel hydraulic diameter (or particle confinement,  $\alpha = d_p/\Phi$ ) (Di Carlo *et al* 2007). These forces may cause lateral migration of particles, and become dominant when the particle Reynolds number ( $\text{Re}_p$ ) increases to the order of 1 (Di Carlo 2009, Zhang *et al* 2016):

$$\text{Re}_p = \text{Re}^* \left( \frac{d_p}{D_h} \right)^2 \quad (9)$$

where  $d_p$  is the particle diameter.

In microfluidic channels, lateral particle migration is governed by the action of (i) a shear gradient lift force due to the curvature of the undisturbed fluid velocity profile (directed towards the channel wall), and (ii) a wall effect lift force due to the asymmetric wake of a particle near the channel wall (directed away from the wall) (Di Carlo 2009, Zhang *et al* 2016). Particle lateral migration is typically observed at  $\alpha > 0.05$  in rectangular microchannels, with migration velocity increasing with increasing particle confinement (Hood *et al* 2016). In this study,  $\text{Re}_p$  in the parent channel is in the range  $5.17 \times 10^{-6}$ – $5.17 \times 10^{-2}$ , and  $\alpha$  is in the range 0.004–0.02. Therefore, the contribution of inertial forces was not taken into account in the numerical model. Additionally, given the 2D nature of the model, and their magnitudes relative to the magnetic force, the effect of gravity and buoyancy were also neglected (buoyancy force =  $\sim 4 \times 10^{-14}$  N, weight =  $\sim 5 \times 10^{-17}$  N). Similarly, given the very low concentrations of microbubbles typically used in the clinic, bubble–bubble interactions were also not considered.

In a laminar flow regime, a smooth, spherical microbubble moving in a Newtonian fluid experiences Stokes’ drag:

$$\mathbf{F}_d = 6\pi\eta R(\mathbf{u} - \mathbf{v}) \quad (10)$$

where  $\eta$  is the dynamic viscosity of the fluid,  $R$  is the microbubble radius,  $\mathbf{v}$  is microbubble velocity and  $\mathbf{u}$  is fluid velocity. The magnetophoretic force  $\mathbf{F}_m$  on a spherical particle suspended in a dielectric fluid and exposed to an external magnetic field  $\mathbf{H}$  is given by:

$$\mathbf{F}_m = 2\pi R^3 \mu_0 \mu_m \frac{\mu_p - \mu_m}{\mu_p + 2\mu_m} \nabla |\mathbf{H}|^2$$

where  $\mu_p$  is the permeability of the particle (Jones 1995, Ghallab 2010), which is defined by  $\mu_p = 1 + \chi_p$ , where the magnetic susceptibility of the material  $\chi_p$  is described by  $\chi_p \mathbf{H} = \mathbf{M}_p$ . The magnetization  $\mathbf{M}_p$  of the superparamagnetic nanoparticles can in turn be described using a Langevin function:  $L(y) = \coth y - 1/y$

$$|M_p| = \beta M_s L \left( \frac{M_s V \mu_0 |\mathbf{H}|}{k_B T} \right) \quad (12)$$

where  $M_s$  is the saturation magnetization of the superparamagnetic nanoparticles,  $V$  is the effective volume of a superparamagnetic nanoparticle,  $\beta$  is the volumetric ratio of superparamagnetic nanoparticles in a microbubble, and  $k_B$  and  $T$  are the Boltzmann constant and temperature, respectively (Bean 1959).

The computational model for microbubble transport was setup as a time-dependent study in time steps of 6 ms over the course of 150 s, which is of the order of the expected half-life of a bolus injection *in vivo* (Mullin *et al* 2011). The trajectories of 300 microbubbles were computed using the ‘Particle Tracing Module’ in COMSOL®. Microbubbles were modelled as individual, spherical, incompressible, air-filled particles. At  $t = 0$  s, a monodisperse population of 300 microbubbles was injected into a steady-state flow and with a uniform distribution along line K (see figure 1(b)).

### 2.3. *In vitro* experiments

A PDMS-glass microfluidic device was used to mimic an arteriolar bifurcation with the same dimensions as the numerical model. To reflect the simulations, three types of experiments were carried out: flow visualization, drug delivery, and microbubble delivery.

**2.3.1. Materials.** Poly(dimethyl-siloxane) (PDMS) was purchased from Dow Corning Corporation (Auburn, MI, USA); epoxy adhesive resin (Yellow Dual Cartridge) from RS Components Ltd (Northants, UK); polyethylene glycol (40) stearate (PEG40S), glycerol, propylene glycol, chloroform, dimethyl sulfoxide (DMSO), and soda-lime glass slides from Sigma Aldrich (Gillingham, UK); 1,2-distearoyl-sn-glycero-3-phosphocholine (DSPC) from Avanti Polar Lipids (Alabaster, AL, USA); sulphur hexafluoride (SF<sub>6</sub>) from the BOC Group (Guildford, UK); phosphate-buffered saline (PBS) and the lipid analogue dye DiI (1,1'-dioctadecyl-3,3,3',3'-tetramethylindocarbocyanine perchlorate) from Thermo Fisher Scientific Inc. (Paisley, UK); and 10 nm diameter lipid-coated iron oxide nanoparticles in aqueous solution from Chemicell (FluidMAG-Lipid, Chemicell GmbH, Berlin, Germany, 25 mg ml<sup>-1</sup>).

**2.3.2. Microfluidic device and experimental setup.** The PDMS-glass microfluidic device was manufactured following a replica molding microfabrication protocol previously described by Carugo *et al* (2016). Briefly, a negative mold of the device was milled into a poly(methylmethacrylate) block. Liquid epoxy adhesive was then poured over the milled block to obtain a positive mold. Liquid PDMS was cast in the positive mold with a curing agent:monomer ratio of 1:10 w/w. The PDMS layer was then cured and bonded to a 1 mm thick glass slide by plasma treatment (plasma cleaner ATTO, Diener electronic GmbH, Ebhausen, Germany). The dimensions of the device are shown in table 1 and figure 2 illustrates the experimental setup. A syringe pump (World Precision Instruments, Hitchin, UK) fitted with a 3 ml syringe (Beckton Dickinson, Oxford, UK) controlled the flow in the device. A custom-built flow-damping reservoir was placed between the pump and the device to reduce flow oscillations, particularly at low injection rates. The magnetic field was applied using a single 12.7 mm cubic permanent magnet element (N52 grade NdFeB, with a measured magnetization value of  $1.09 \times 10^6$  A m<sup>-1</sup>, CMS Magnetics, Garland, TX, USA (Barnsley *et al* 2015). The magnet was placed in the same position as in the simulations, with its magnetization vector parallel to line M and its surface 10 mm away from the center of the bifurcation (point Y). The base of the magnet was flush with the glass slide.

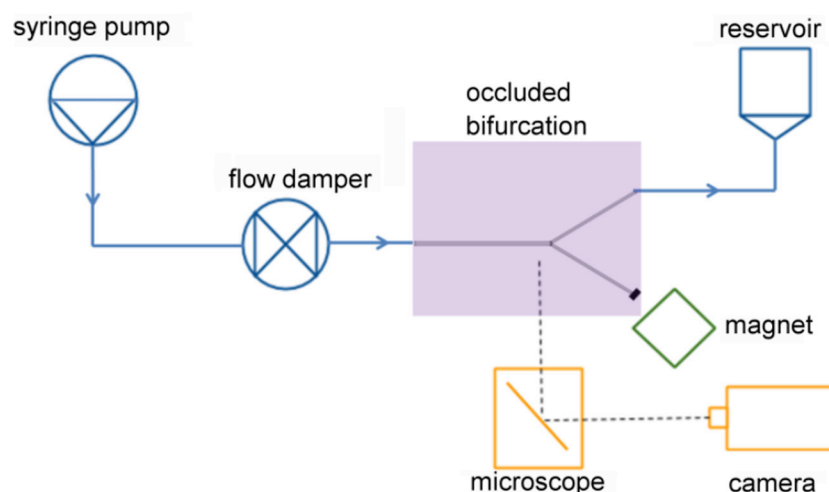


**Figure 2.** Schematic of the experimental setup. A syringe pump was employed to control flow rates into a microfluidic bifurcation with a fully occluded branch. A cubic permanent magnet provided the magnetic field. A fluorescence microscope enabled real-time imaging of FITC-labelled beads (flow visualization study), TRITC-tagged bovine serum albumin (drug delivery study), and DiI-labelled magnetic microbubbles (microbubble delivery study).

**2.3.3. Flow visualization.** In the flow visualization experiments,  $2\ \mu\text{m}$  diameter fluorescein-labelled polystyrene beads (Sigma Aldrich) were used as flow tracers, and suspended in water at a concentration of  $1.5 \times 10^8$  particles  $\text{ml}^{-1}$ . Images of the bifurcation region were acquired on a fluorescence microscope (Ti Eclipse, Nikon Instruments Inc., NY, USA) with a  $10\times$  magnification objective (Plan Fluor Ph1 DLL, Nikon) and a digital camera (Digital Sight Qi1Mc-U2, Nikon). The excitation and emission wavelengths were 470 nm and 510–550 nm respectively, the frame rate was set to  $14\ \text{frames s}^{-1}$ , and the camera exposure time ranged from 2 to 67 ms.

**2.3.4. Drug delivery.** In the drug delivery experiments, fluorescent bovine serum albumin was used as a model for tPA (TRITC-BSA, Thermo Fisher Scientific), as it is a globular protein with a similar molecular weight (Young *et al* 1980, Tyn and Gusek 1990). The model drug was injected at a final concentration of  $6.2 \times 10^{-8}$  mol  $\text{l}^{-1}$  in deionized water. Microscopic data acquisition began immediately after flow initiation, with fluorescence excitation set at 470 nm, acquisition between 510 and 550 nm, and a  $10\times$  objective. A tile scan of the whole occluded branch was performed every 30 s to monitor drug diffusion, with an exposure time of 333 ms. Microscope images were processed with a custom-built code written in Matlab (The MathWorks Inc., Natick, MA, USA) to yield a grayscale profile along a 10-pixel wide line with the same coordinates as line M.

**2.3.5. Microbubble delivery.** In the microbubble delivery experiments, lipid-shelled microbubbles loaded with iron oxide nanoparticles were labelled with the lipid analogue dye DiI for visualization and tracking. To prepare the microbubbles, DSPC and PEG40 stearate, dissolved in chloroform, were mixed in a glass vial in a 9:1 molar ratio, and  $50\ \mu\text{g}$  of DiI dissolved in DMSO was added. The solvent was then allowed to evaporate at  $50\ ^\circ\text{C}$  for 12 h. A solution of PBS, glycerol and propylene glycol was prepared with a volume ratio of 8:1:1 and the lipid film was re-suspended in 2 ml of this solution for approximately 1 h at  $75\ ^\circ\text{C}$  under constant stirring. The preparation was then sonicated for 90 s using a 22.5 kHz ultrasonic cell disruptor

(Microson XL, Misonix Inc., Farmingdale, NY, USA) operating at level 4, corresponding to a root mean square (rms) output power of 8 W. During sonication, the tip of the sonicating probe was fully immersed in the solution. 15  $\mu\text{l}$  of the iron oxide nanoparticle solution were added for the final 30 s of sonication. This was followed by a second sonication step under positive pressure of  $\text{SF}_6$  at level 19 for 20 s, with the sonicating tip placed at the gas–water interface to entrain gas. The microbubble solution was then cooled in an ice bath for approximately 10 min. Microbubble size and concentration were measured by bright field microscopy as previously described by Sennoga *et al* (2010). For the delivery experiments, microbubble concentration was then adjusted with PBS to  $2.9 \times 10^8$  microbubbles  $\text{ml}^{-1}$ . Microbubbles were washed once by centrifugation (300 RCF, for 10 min) to remove excess DiI.

Image acquisition was performed using the same fluorescence microscope as above at  $10\times$  magnification, with fluorescence excitation at 525 nm, acquisition between 575 and 625 nm, and an exposure time of 50 ms. The final microbubble distribution was investigated with scans of the whole occluded branch in the mid-plane of the channel. These images were processed using a purpose-written code in Matlab to yield an average brightness profile along the occluded branch.

### 3. Results

#### 3.1. Flow dynamics

The first stage of the investigation explored the fluid dynamic phenomena that develop in the cavity formed by the occluded branch.

**3.1.1. Numerical simulations.** In the numerical model, the flow field in the channel was computed and the influence of inlet velocity was investigated, as well as the effect of clot position along the occluded branch (i.e. branch length). The inset in figure 3(a) shows an example of the flow pattern in the occluded branch. Multiple counter-rotating vortices formed and fluid velocity along the midline of the branch dropped rapidly (by 94% within 150  $\mu\text{m}$  of the bifurcation point). Fluid velocity along the midline of the branch increased with inlet velocity (or Reynolds number) (figure 3(b)), but was not affected by branch length (figure S2). As a result, only the effect of inlet velocity was examined. In addition, it was noted that neither parameter affected the position or size of the vortices.

**3.1.2. *In vitro* experiments.** Figure 4 shows the flow pattern in the bifurcation, observed by fluorescence microscopy using flow tracers. In the parent branch and in the free branch, flow velocity was such that individual tracers could not be distinguished. In the occluded branch, the first vortex was clearly visible: flow velocity was lower in this region and individual streaks were observed. The subsequent vortices, characterized by a significantly lower velocity, could not be observed experimentally using the same acquisition settings. The experiment was repeated at all four mean inlet velocities and the flow patterns were found to be comparable (data not shown). The predicted flow pattern and the experimental observations were similar in the first vortex. Small differences in the location of the vortex center can be attributed to the 2D nature of the simulations.

#### 3.2. Drug delivery

The transient phase of tPA delivery in the bifurcation was investigated. Continuous infusion of a clinically relevant concentration of tPA was simulated and drug distribution in the following 60 min was modelled. tPA delivery was also observed *in vitro* using a fluorescent drug model

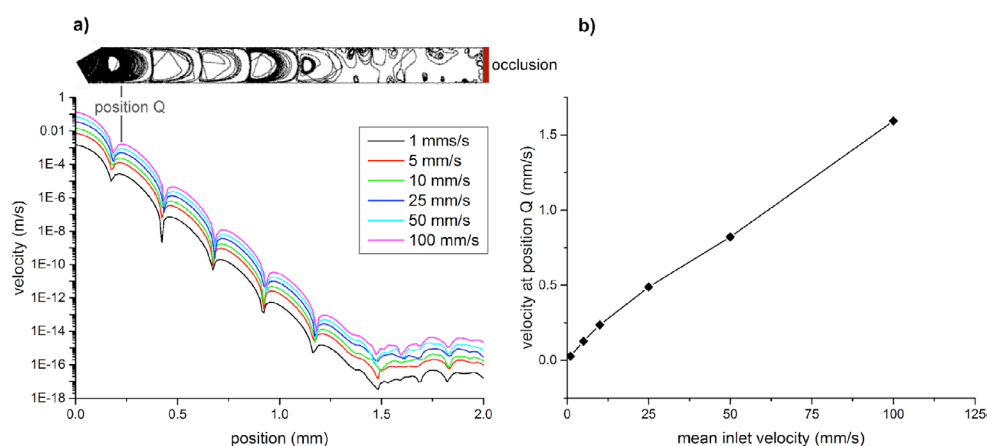


**Figure 3.** Influence of mean inlet velocity on the flow field in the occluded branch. (a) Fluid velocity along the axis of the occluded branch (line M) for six mean inlet velocities in the 1–100 mm s<sup>-1</sup> range (corresponding to a Reynolds number in the range 0.25–25). Fluid velocity is plotted as a function of position along line M, with the origin at point Y. Inset (above): streamlines in the occluded branch at corresponding positions. (b) Velocity at position marked Q in subfigure (a), as a function of mean inlet velocity. In this simulation, occluded branch length = 2 mm.

(TRITC-labelled BSA). The simulation results shown in figure 5 indicate that drug delivery to the occluded vessel was limited: after 60 min of continuous infusion, the concentration at 1.64 mm from the center of the bifurcation was only 5% of the parent vessel concentration. Similarly, in the experimental model, fluorescence intensity decreased rapidly as the distance from the bifurcation increased. It reached 5% of the main vessel intensity within 930  $\mu\text{m}$ . In order to analyze the changes in concentration, a ‘half concentration distance’ was defined as the distance along line M at which drug concentration reaches half of the injected concentration. The numerical simulations showed that this half concentration distance increased with mean inlet velocity (figure 6).

### 3.3. Microbubble delivery

**3.3.1. Numerical simulations.** In order to quantify microbubble delivery, four possible states were defined for an individual microbubble passing through the bifurcation: (i) *undelivered*, i.e. the microbubble did not reach the bifurcation within the experimental time frame (marked red in figure 7); (ii) *bypassed* the occluded branch and travelled into the free branch (marked blue); (iii) *trapped* in the occluded branch (yellow); and (iv) *delivered* to the clot (green).

**3.3.1.1. Challenges to microbubble delivery in the occluded bifurcation.** Figure 7(a) provides an example of simulated delivery trajectories (black lines) and end-position (colored circles) 150 s after bubble injection in the absence of a magnetic field. The flow rate was 10 mm s<sup>-1</sup> (corresponding to Re of 2.2) and microbubble diameter was 1.2  $\mu\text{m}$ , which is coherent with our experimental determinations and with previous studies reporting on the production of magnetic microbubbles (Mulvana 2012). The majority of microbubbles (296/300 microbubbles, or 98.7%) bypassed the occlusion altogether. 3 microbubbles (1.0%) were trapped in the occluded branch, where they all remained confined to the first fluid vortex, within 350  $\mu\text{m}$  from the bifurcation centre. No microbubble escaped the vortex, and none was delivered to the clot.

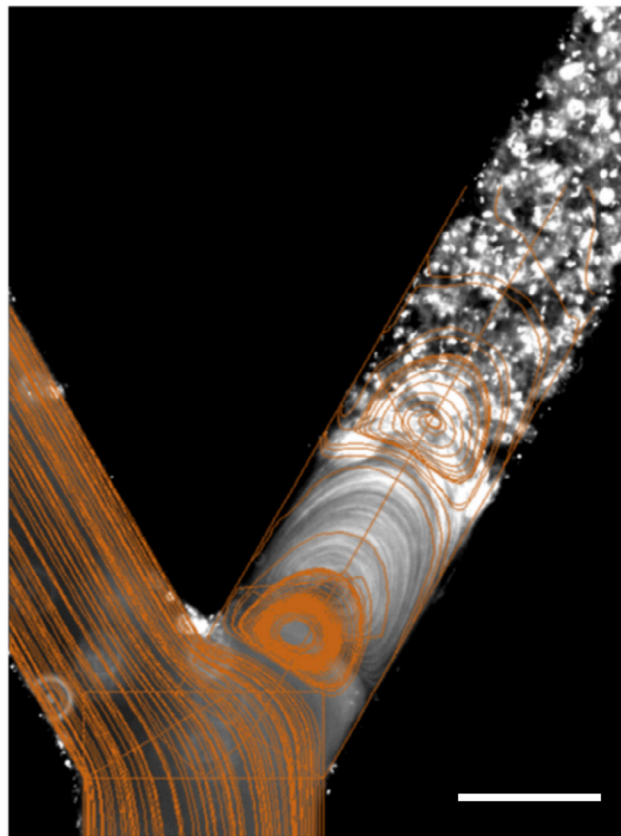


**Figure 4.** Experimental flow pattern in the occluded branch, visualized under fluorescence microscopy using relatively long exposure times (3.4 s), and FITC-labelled microbeads as flow tracers. Numerically computed streamlines are overlaid in orange. Scale bar = 150  $\mu\text{m}$ .

**3.3.1.2. Effect of magnetic targeting on microbubble delivery.** Figure 7(b) illustrates microbubble delivery under the same flow conditions, in the presence of a magnetic field. In this case as well, the majority of microbubbles (285, or 95.0%) bypassed the occluded branch, but 7 microbubbles (2.3%) were trapped in the occluded branch. More importantly, all these microbubbles escaped the first fluid vortex and followed a trajectory close to a straight line. None of them reached the clot, located 8 mm away from the bifurcation point, within the first 150 s of simulation time. However, given that these microbubbles were subject only to the magnetophoretic force and to a very low drag force (fluid velocity is negligible past the first vortex), it is to be expected that they would all reach the clot at a later time point.

**3.3.1.3. Influence of mean inlet velocity on targeted delivery.** Since flow conditions vary within vascular networks, the influence of mean inlet velocity on microbubble delivery was then investigated with and without magnetic targeting for 1.2  $\mu\text{m}$  diameter microbubbles, the average size of the experimental microbubble population (Owen *et al* 2015). Figure 8 shows delivery outcomes 150 s after injection at mean inlet velocities within the clinically relevant range of 1–100  $\text{mm s}^{-1}$  (corresponding to Re in the range 0.22–22.2). In the absence of a magnetic field, the proportion of microbubbles trapped in the occluded branch was very low, regardless of the

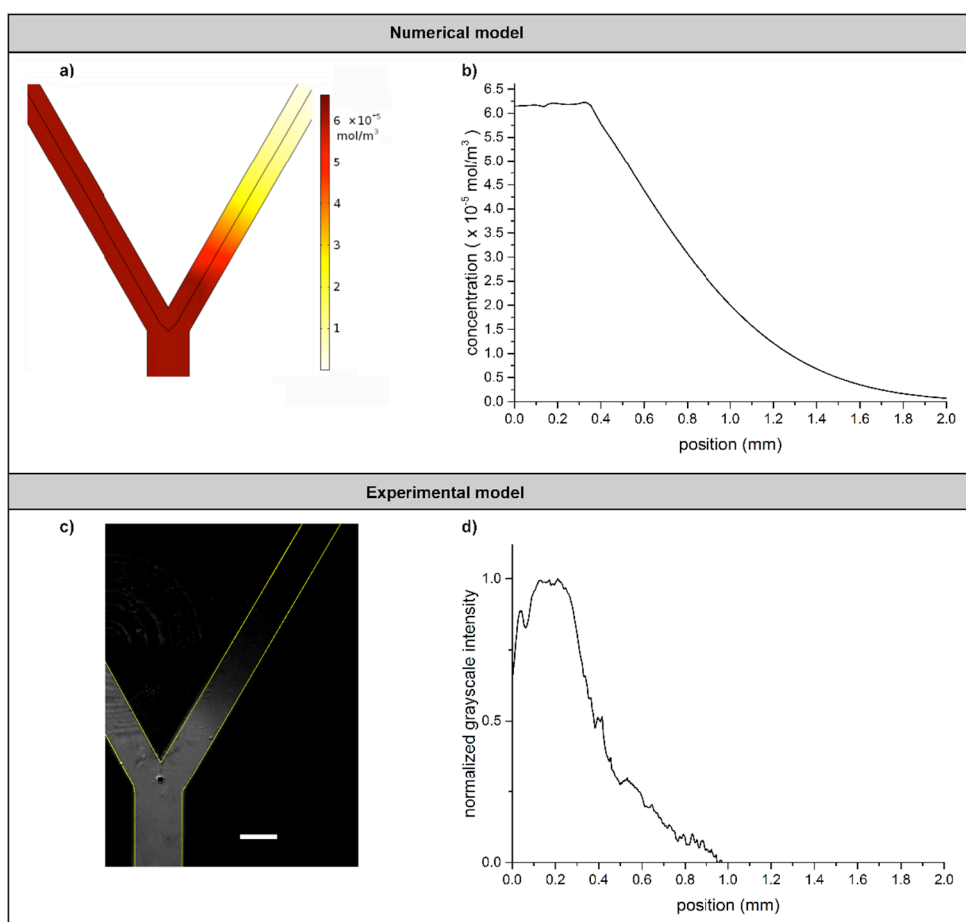


**Figure 5.** Drug distribution in the bifurcation after 1 h of continuous tPA infusion at a concentration of  $6.2 \times 10^2 \text{ mol l}^{-1}$ . (a) Simulated heat map of final tPA concentration in both branches; (b) simulated final concentration of tPA along line M; (c) fluorescence microscopy image of drug distribution in the occluded branch in the experimental model (scale bar =  $250 \mu\text{m}$ ); (d) normalized greyscale intensity along line M in the experimental model. In all cases, mean inlet velocity =  $10 \text{ mm s}^{-1}$  (Reynolds number = 2.2) and branch length = 8 mm. In subfigures (a) and (c), only the bifurcation region is shown. Both branches extend well beyond the first section represented here.

mean inlet velocity (below 2%). In the presence of a magnetic field, a marked increase in the number of trapped microbubbles was observed at all inlet fluid velocities (depending on mean fluid velocity, an increase of between 125% and 465%, i.e. 4 to 14 additional microbubbles out of 300). The proportion of microbubbles trapped with the magnet was sensitive to the mean inlet velocity and, as might be expected, tended to decrease with increasing velocity. Figure 8(b) also highlights another phenomenon: at low velocities and in the presence of a magnetic field, a large proportion of microbubbles (up to 10% at  $1 \text{ mm s}^{-1}$ ) remained undelivered. They were pulled by the magnet close to the parent branch wall, where flow velocity is slower, and as a result did not reach the bifurcation within the simulation time. This effect decreased rapidly with increasing fluid velocity. As in the previous section, no microbubbles of this size reached the clot within the short simulation timeframe, regardless of mean inlet velocity.

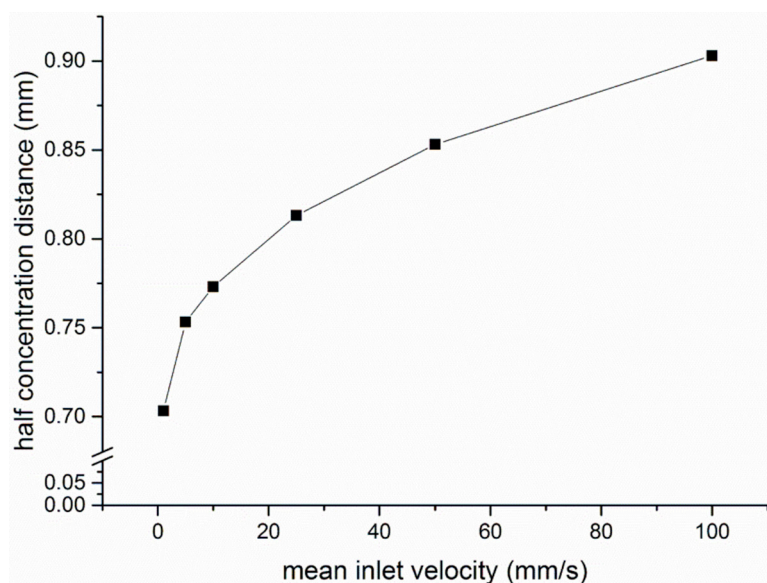


**Figure 6.** Effect of mean inlet velocity on half concentration distance along line *M* at  $t = 60$  min, during continuous tPA infusion at a concentration of  $6.2 \times 10^2 \text{ mol l}^{-1}$  (simulation results, branch length = 8 mm). Reynolds number ranges from 2.2 to 22.2.

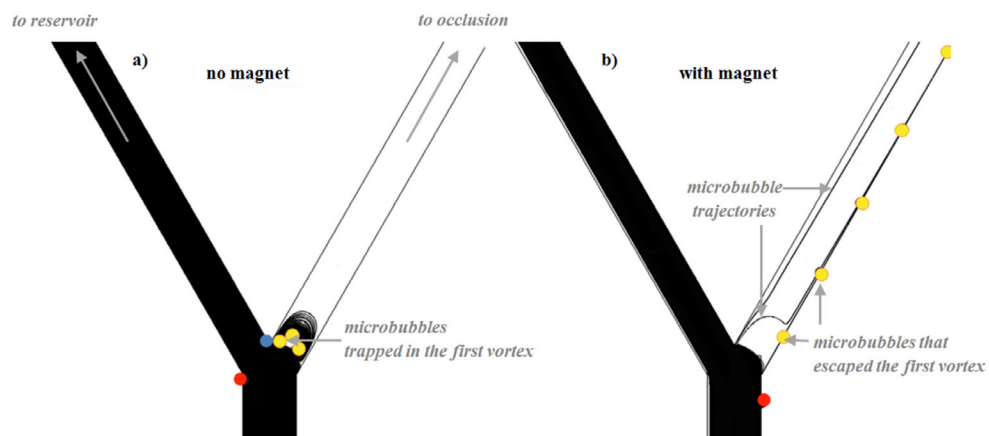


**Figure 7.** Example of simulated microbubble delivery at  $t = 150$  s after injection: (a) without magnetic field and (b) with magnetic field. Black lines correspond to individual microbubble trajectories, colored circles show final microbubble position (red = undelivered, blue = bypassed, yellow = trapped, green = delivered). Both branches extend well beyond the first section represented here. In this simulation, mean inlet velocity =  $10 \text{ mm s}^{-1}$  ( $Re = 2.2$ ), microbubble diameter =  $1.2 \mu\text{m}$ , branch length = 8 mm.

**3.3.1.4. Influence of microbubble size on targeted delivery.** Microbubbles of various sizes experience different drag and magnetophoretic forces, and the formulation can therefore be engineered to optimize bubble size for delivery. The effect of size on delivery was therefore investigated by simulating trajectories for microbubbles within a  $0.6\text{--}5 \mu\text{m}$  diameter range, which is comparable to the size range of commercially available contrast agents (Mulvana

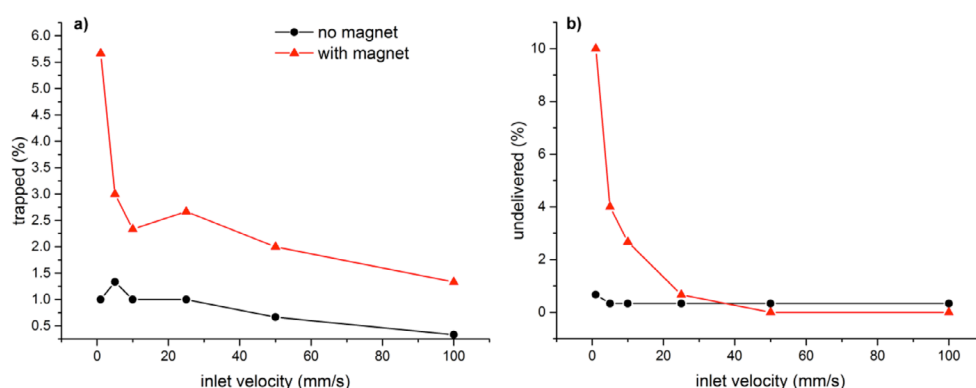


**Figure 8.** Simulated effect of mean inlet velocity and magnetic targeting on microbubble distribution after 150s simulation time: (a) the proportion of microbubbles trapped in the occluded branch; (b) the proportion of undelivered microbubbles. In this case, microbubble diameter =  $1.2 \mu\text{m}$  and branch length = 8 mm.

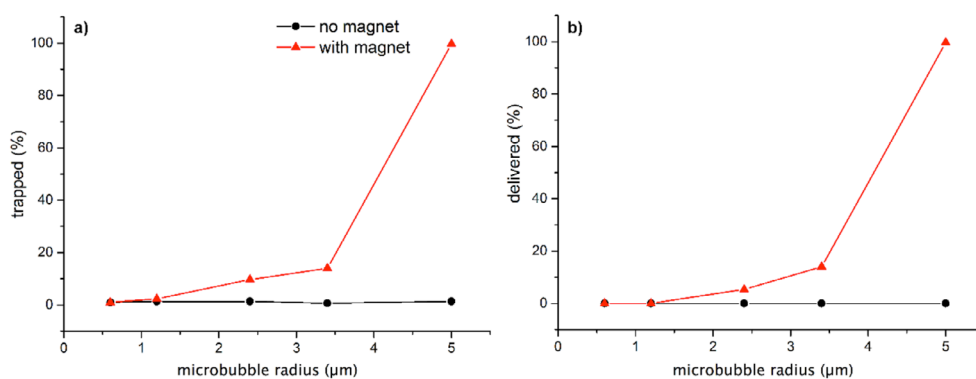


**Figure 9.** Simulated effect of mean microbubble diameter and magnetic targeting on microbubble position after 150s simulation time: (a) the proportion of microbubbles trapped in the occluded branch; (b) the proportion of microbubbles delivered to the clot, 8 mm into the occluded branch. In these simulations, mean inlet velocity =  $10 \text{ mm s}^{-1}$  (corresponding to  $\text{Re}$  of 2.2) and branch length = 8 mm.

*et al* 2012). Figure 9 shows the outcomes for five different microbubble sizes. In the absence of a magnetic field, size had no effect on delivery outcomes. At all sizes, fewer than 2% of the injected microbubbles were trapped in the occluded branch. On the other hand, in the presence of a magnetic field, microbubble delivery was enhanced, and the outcome was highly sensitive to size due to increased magnetic force for the larger microbubbles. The proportion of microbubbles trapped and delivered increased rapidly with microbubble diameter, from 1% trapped and 1.7% delivered at  $0.6 \mu\text{m}$  to 100% trapped and delivered at  $5 \mu\text{m}$ .

**3.3.2. In vitro experiments.** Microbubble distribution was investigated experimentally in the microfluidic bifurcation at various mean inlet velocities (or inlet Reynolds numbers) in the presence and in the absence of a magnet. Figures 10 and S3 show delivery outcomes in the mid-plane of the occluded branch, at different inlet mean velocities (in the range  $5\text{--}50 \text{ mm s}^{-1}$ ). For instance, at  $5 \text{ mm s}^{-1}$  mean inlet velocity (Reynolds number = 1.1, figure 10), a 1.4-fold increase in total grayscale intensity was observed in the occluded branch in the

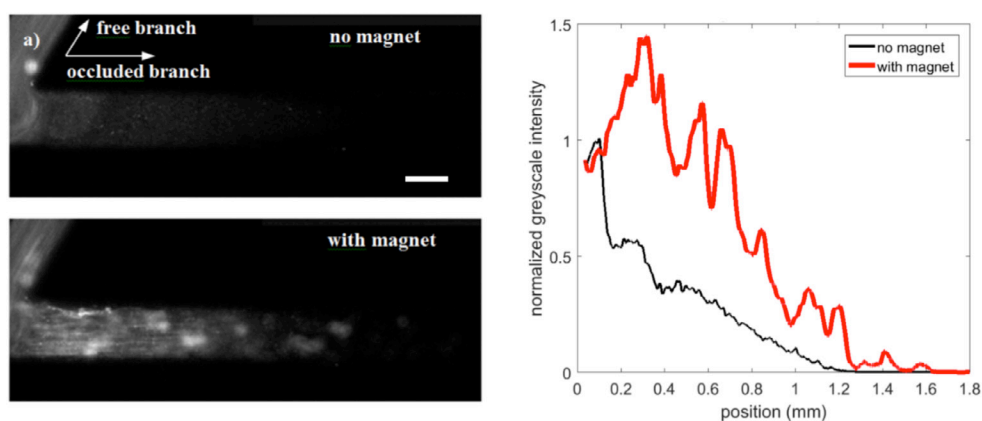


**Figure 10.** Experimental effect of a magnetic field on the delivery of DiI-labelled magnetic microbubbles with  $5 \text{ mm s}^{-1}$  mean inlet velocity (corresponding to  $\text{Re} = 1.1$ ). (a) Fluorescence microscopy image of the mid-plane of the occluded branch at  $t = 10 \text{ min}$  (scale bar =  $150 \mu\text{m}$ ); (b) grayscale intensity profile along the occluded branch at  $t = 10 \text{ min}$ , normalized to the mean grayscale intensity at the bifurcation center.

presence of a magnetic field, and the microbubbles were delivered up to  $385 \mu\text{m}$  away from the entrance of the occluded branch.

#### 4. Discussion and conclusions

To the best of the authors' knowledge, this is the first investigation of magnetic targeting to enhance particle delivery in fully occluded microvascular models. Drug diffusion in occluded bifurcations has been previously investigated in other physiological or therapeutic contexts. For instance, Carugo *et al* modelled the flow field and doxorubicin distribution in a bifurcation occluded by a drug-eluting chemoembolic bead, and revealed how vortical flow in the embolised microvessel can locally enhance drug elution (Carugo *et al* 2015). Verhaagen *et al* investigated drug distribution in a fully occluded side-channel during antimicrobial treatment of the root canal. Numerical and experimental data showed that flow in the main canal induces a cascade of vortices in the lateral microchannel, with rapidly decreasing velocities. They also noted that beyond the opening region of the channel, drug transport is slow and diffusion-dominated (Verhaagen *et al* 2014). These observations were consistent with the present study.

Inertial particle migration and cavity flow in microchannels have been investigated as a means to trap biological cells or microparticles, for applications including cell isolation and sample enrichment (Hur *et al* 2011, Sollier *et al* 2014). Notably, lateral migration of particles due to shear gradient lift forces can be employed to drive particles into cavities positioned side-wise, where they are trapped within laminar vortices formed within the cavity. Critical particle diameter for trapping has been observed to be in the range  $5\text{--}10 \mu\text{m}$  (for rigid microspheres), and trapping of  $10 \mu\text{m}$  particles initiated only at Reynolds number of 130. Smaller particles (i.e.  $5 \mu\text{m}$  in diameter) were not trapped even at  $\text{Re} > 240$  (Hur *et al* 2011). Moreover, a larger shear-gradient lift force would be required to direct deformable particles into a vortex, as opposed to rigid particles.

Given the microbubble size (maximum diameter =  $5 \mu\text{m}$ ) and Reynolds number (maximum  $\text{Re} = 25$ ) employed in this study, inertial focusing of microbubbles in the parent channel

was not observed, and a very small proportion of microbubbles was directed into the vortex formed by the occlusion. Only microbubbles with an initial lateral position close to the channel sidewall (towards the occluded branch) were trapped into the vortex in the absence of a magnetic field. Upon trapping, they did not leave the vortex since no external force was applied to overcome fluid drag.

In the presence of a magnetic field, a higher proportion of microbubbles were directed into the occluded microchannel. These can be categorized into two groups; the first group includes microbubbles with an initial lateral position close to the channel sidewall (towards the occluded branch). These microbubbles entered the occluded channel in a proximal position and moved along its sidewall where the drag force is lower (due to the associated low fluid velocity). The second group includes microbubbles entering the distal extremity of the vortex (i.e. close to the apex of the bifurcation), and exiting at a point where the magnetic force overcomes the drag force. They again escaped the vortex at its periphery, due to the lower drag force in this region. More distal vortices within the occluded branch did not appear to have an effect on particle trajectory, and this is likely due to the rapid and significant reduction in fluid velocity along the occluded microchannel. Larger microbubbles experienced a higher magnetic force, and thus a significantly higher proportion of these was directed towards the occlusion. Clustering of microbubbles occurred in some cases (see figure 10), most likely owing to the low shear gradient within the vortex or the magnetic field. However, clustering is not permanent and should not impact on the behaviour of microbubbles entering the occluded channel.

The numerical simulations and *in vitro* experiments showed good qualitative agreement. Minor differences may be attributed in part to 3D effects not taken into account by the 2D numerical simulations, and to residual pulsatility of the pump. More significantly, the amount of magnetic material on a microbubble is difficult to measure experimentally and was therefore necessarily approximated in the computational model. In addition, the use of greyscale intensities to evaluate delivery outcomes must be qualified. Though greyscale intensities are appropriate to observe trends in microbubble delivery, they do not translate directly into microbubble numbers, as a small amount of free DiI may still be present in the solution after centrifugation and it may diffuse into the occluded branch alongside DiI-labelled microbubbles.

The observations reported in this study could provide valuable guidance for clinical translation of magnetically targeted sonothrombolysis. Notably, requirements can be formulated for a clinically relevant magnetic targeting system. Magnetic microbubbles were successfully delivered to the clot with a magnetic flux density of 76 mT and a magnetic flux density gradient of  $10.90 \text{ T m}^{-1}$  at the bifurcation point (point Y). In the current state of the art, the required flux density and flux density gradient are possible with permanent magnet arrays at depths up to 40 mm into the body (Barnsley *et al* 2015). As regards the clinical relevance of the model itself, as described above, the lengthscales and flow rates were selected to be representative of conditions found in ST elevation myocardial infarctions. Clearly, however, there are some significant simplifications. Importantly, the presence of red blood cells has been ignored and this has been shown in previous work to influence the retention of microbubbles by a magnetic field in 200  $\mu\text{m}$  diameter vessels (Owen *et al* 2014). Physiological flow pulsatility and vessel wall compliance were also neglected, and these may introduce a time dependent component to the flow field that will also affect microbubble delivery. The authors intend to investigate these phenomena in future work, and also to address the case of a partially occluded branch. This corresponds to conditions during treatment once the thrombus has been partially lysed and to other pathologies for which microbubble mediated therapy may be applicable.

It is recognized that using magnetic targeting to navigate particles through the vasculature is incredibly challenging, owing to its ramified structure (Grief and Richardson 2005, Cherry

and Eaton 2014). In particular, when using a magnet to apply a pull force to navigate particles through branching vessels, the target branch must be between the magnetic field source and the injection point (Grief and Richardson 2005, Shapiro *et al* 2015), as the greatest proportion of particles will typically accumulate in the branches that experience the highest magnetic force. Additionally, for many common magnetic geometries, the magnitude of the magnetic force decays almost exponentially with distance (Hayden and Häfeli 2006). This means that, for a protocol to work efficiently, the design and alignment of the magnet is of critical importance during therapy, so that the optimal magnitude and force can be delivered to the target. This problem can be expedited by active imaging of the particles and target during treatment.

Moreover, although the arteriolar model developed in the present study had a physiologically relevant size, a broad range of vessel diameters can be found *in vivo*, and the vessel size may affect microbubble behaviour upon magnetic targeting. Higher Reynolds number will typically occur in larger vessels (i.e. small arteries). Carugo has modelled fluid flow in an occluded bifurcation, with a parent vessel width of 600  $\mu\text{m}$ . They have shown that vortex size and velocity in the occluded branch increase with increasing Reynolds number in the parent branch from 200 to 850 (Carugo 2012). Increased vortex velocity and size may reduce the percentage of targeted microbubbles for a specific magnetic field strength, given the higher drag force and microbubble velocity within the vortex.

Blood flow in smaller arterioles (i.e. diameter < 100  $\mu\text{m}$ ) will instead have a lower Reynolds number, which will result in a lower drag force within the vortex. Trapping efficiency is expected to increase under these conditions. However, microbubble confinement may also become relevant in the smaller microvessels, which may influence microbubble radial position in the parent vessel and therefore the percentage of microbubbles delivered to the clot.

In conclusion, this study has examined the challenges involved in delivering therapeutic agents to occluded microvessels. The results show that magnetic targeting has the potential to increase delivery efficacy of microbubbles and that the magnetic field required is achievable at clinically relevant tissue depths. The approach thus has potential to improve treatment of stroke, myocardial infarction and other occlusive conditions.

## Acknowledgments

The authors gratefully acknowledge the assistance of James Fisk and David Salisbury in fabricating the microfluidic device. The authors thank the EPSRC for funding the research under grant EP/I021795/1 and the Research Council UK Digital Economy Programme, Centre for Doctoral Training in Healthcare Innovation (grant EP/G036861/1).

## ORCID iDs

L C Barnsley  <https://orcid.org/0000-0002-1341-905X>

E Stride  <https://orcid.org/0000-0003-3371-5929>

## References

- Alexandrov A V *et al* 2008 A pilot randomized clinical safety study of sonothrombolysis augmentation with ultrasound-activated perflutren-lipid microspheres for acute ischemic stroke *Stroke* **39** 1464–9
- American College of Emergency Physicians and American Academy of Neurology 2013 Clinical policy: use of intravenous tPA for the management of acute ischemic stroke in the emergency department *Ann. Emerg. Med.* **61** 225–43

- Anderson J L 1997 Why does thrombolysis fail? Breaking through the reperfusion ceiling *Am. J. Cardiol.* **80** 1588–90
- Barnsley L C, Carugo D, Owen J and Stride E 2015 Halbach arrays consisting of cubic elements optimised for high field gradients in magnetic drug targeting applications *Phys. Med. Biol.* **60** 8303–27
- Bean C P L and Livingston J D 1959 Superparamagnetism *J. Appl. Phys.* **30** 10
- Belyaev A V, Panteleev M A and Ataullakhanov F I 2015 Threshold of microvascular occlusion: injury size defines the thrombosis scenario *Biophys. J.* **109** 450–6
- Borrelli M J, O'Brien W D, Hamilton E, Oelze M L, Wu J, Bernock L J, Tung S, Rokadia H and Culp W C 2012 Influences of microbubble diameter and ultrasonic parameters on *in vitro* sonothrombolysis efficacy *J. Vasc. Intervent. Radiol.* **23** 1677–84
- Brown A T, Flores R, Hamilton E, Roberson P K, Borrelli M J and Culp W C 2011 Microbubbles improve sonothrombolysis *in vitro* and decrease hemorrhage *in vivo* in a rabbit stroke model *Investigative Radiol.* **46** 202–7
- California Acute Stroke Pilot Registry Investigators 2005 Prioritizing interventions to improve rates of thrombolysis for ischemic stroke *Neurology* **64** 654–9
- Carugo D 2012 Development of microfluidic systems for therapeutic applications *PhD Thesis* University of Southampton (<https://eprints.soton.ac.uk/348835/>)
- Carugo D, Capretto L, Roy B, Carboni M, Caine M, Lewis A L, Hill M, Chakraborty S and Zhang X 2015 Spatiotemporal dynamics of doxorubicin elution from embolic beads within a microfluidic network *J. Control. Rel.* **214** 62–75
- Carugo D, Lee J Y, Pora A, Browning R J, Capretto L, Nastruzzi C and Stride E 2016 Facile and cost-effective production of microscale PDMS architectures using a combined micromilling-replica moulding ( $\mu$  Mi-REM) technique *Biomed. Microdevices* **18** 4
- Cherry E M and Eaton J K 2014 A comprehensive model of magnetic particle motion during magnetic drug targeting *Int. J. Multiph. Flow* **59** 171, 173–85
- Chesebro J H *et al* 1987 Thrombolysis in myocardial-infarction (Timi) trial, phase-I—a comparison between intravenous tissue plasminogen-activator and intravenous streptokinase—clinical findings through hospital discharge *Circulation* **76** 142–54
- Chikazumi S 1997 *Physics of Ferromagnetism* vol 1 (Oxford: Oxford University Press)
- Culp W C, Porter T R, Xie F, Goertzen T C, McCowan T C, Vonk B N and Baxter B T 2001 Microbubble potentiated ultrasound as a method of declotting thrombosed dialysis grafts: experimental study in dogs *Cardiovasc. Intervent. Radiat.* **24** 407–12
- Di Carlo D 2009 Inertial microfluidics *Lab Chip* **9** 3038–46
- Di Carlo D, Irimia D, Tompkins R G and Toner M 2007 Continuous inertial focusing, ordering, and separation of particles in microchannels *Proc. Natl Acad. Sci. USA* **104** 18892–7
- Feigin V L, Lawes C M M, Bennett D A and Anderson C S 2003 Stroke epidemiology: a review of population-based studies of incidence, prevalence, and case-fatality in the late 20th century *Lancet Neurol.* **2** 43–53
- Fung Y 1997 *Biomechanics: Circulation* (New York: Springer)
- Ghallab Y H B and Badawy W 2010 *Lab-on-a-Chip: Techniques, Circuits, and Biomedical Applications* (Boston, MA: Artech House Publishers)
- Grief A D and Richardson G 2005 Mathematical modelling of magnetically targeted drug delivery *J. Magn. Magn. Mater.* **293** 455
- Hacke W *et al* 2008 Guidelines for management of ischaemic stroke and transient ischaemic attack 2008—The European Stroke Organisation (ESO) Executive Committee and the ESO Writing Committee *Cerebrovasc. Dis.* **25** 457–507
- Hayden M E and Häfeli U O 2006 'Magnetic bandages' for targeted delivery of therapeutic agents *J. Phys.: Condens. Matter* **18** S2877
- Hood K, Kahkeshani S, Di Carlo D and Roper M 2016 Direct measurement of particle inertial migration in rectangular microchannels *Lab Chip* **16** 2840–50
- Hur S C, Mach A J and Di Carlo D 2011 High-throughput size-based rare cell enrichment using microscale vortices *Biomicrofluidics* **5** 22206
- Jain A, Graveline A, Waterhouse A, Vernet A, Flaumenhaft R and Ingber D E 2016 A shear gradient-activated microfluidic device for automated monitoring of whole blood haemostasis and platelet function *Nat. Commun.* **7** 10176
- Jones T 1995 *Electromechanics of Particles* (Cambridge: Cambridge University Press)
- Kern R, Diels A, Pettenpohl J, Kablau M, Brade J, Hennerici M G and Meairs S 2011 Real-time ultrasound brain perfusion imaging with analysis of microbubble replenishment in acute MCA stroke *J. Cereb. Blood Flow Metab.* **31** 1716–24

- Matuskova J, Chauhan A K, Cambien B, Astrof S, Dole V S, Piffath C L, Hynes R O and Wagner D D 2006 Decreased plasma fibronectin leads to delayed thrombus growth in injured arterioles *Arterioscler., Thromb., Vasc. Biol.* **26** 1391–6
- Molina C A *et al* 2009 Transcranial ultrasound in clinical sonothrombolysis (TUCSON) trial *Ann. Neurol.* **66** 28–38
- Mullin L, Gessner R, Kwan J, Kaya M, Borden M A and Dayton P A 2011 Effect of anesthesia carrier gas on *in vivo* circulation times of ultrasound microbubble contrast agents in rats *Contrast Media Mol. Imaging* **6** 126–31
- Mulvana H, Eckersley R J, Tang M X, Pankhurst Q and Stride E 2012 Theoretical and experimental characterisation of magnetic microbubbles *Ultrasound Med. Biol.* **38** 864–75
- Ni H, Denis C V, Subbarao S, Degen J L, Sato T N, Hynes R O and Wagner D D 2000 Persistence of platelet thrombus formation in arterioles of mice lacking both von Willebrand factor and fibrinogen *J. Clin. Invest.* **106** 385–92
- Ni H, Yuen P S, Papalia J M, Trevithick J E, Sakai T, Fassler R, Hynes R O and Wagner D D 2003 Plasma fibronectin promotes thrombus growth and stability in injured arterioles *Proc. National Academy of Sciences of the United States of America* **100** 2415–9
- Owen J, Grove P, Rademeyer P and Stride E 2014 The influence of blood on targeted microbubbles *J. R. Soc. Interface* **11** 20140622
- Owen J, Rademeyer P, Chung D, Cheng Q, Holroyd D, Coussios C, Friend P, Pankhurst Q A and Stride E 2015 Magnetic targeting of microbubbles against physiologically relevant flow conditions *Interface Focus* **5** 20150001
- Perren F, Loulidi J, Pogliani D, Landis T and Sztajzel R 2008 Microbubble potentiated transcranial duplex ultrasound enhances IV thrombolysis in acute stroke *J. Thromb. Thrombolysis* **25** 219–23
- Petit B, Gaud E, Colevret D, Arditi M, Yan F, Tranquart F and Allemann E 2012 *In vitro* sonothrombolysis of human blood clots with BR38 microbubbles *Ultrasound Med. Biol.* **38** 1222–33
- Rezkalla S H and Kloner R A 2002 No-reflow phenomenon—response *Circulation* **106** E143
- Sennoga C A, Mahue V, Loughran J, Casey J, Seddon J M, Tang M and Eckersley R J 2010 On sizing and counting of microbubbles using optical microscopy *Ultrasound Med. Biol.* **36** 2093–6
- Shapiro B *et al* 2015 Open challenges in magnetic drug targeting *Wiley Interdiscip. Rev. Nanomed. Nanobiotechnol.* **7** 446
- Sherman T F 1981 On connecting large vessels to small. The meaning of Murray's law *J. Gen. Physiol.* **78** 431–53
- Sollier E *et al* 2014 Size-selective collection of circulating tumor cells using Vortex technology *Lab Chip* **14** 63–77
- Tehrani M D, Yoon J H, Kim M O and Yoon J 2015 A novel scheme for nanoparticle steering in blood vessels using a functionalized magnetic field *IEEE Trans. Biomed. Eng.* **62** 303–13
- The National Institute of Neurological Disorders and Stroke rt-PA Stroke Study Group 1995 Tissue plasminogen activator for acute ischemic stroke *New Engl. J. Med.* **333** 1581–7
- Torno M D, Kaminski M D, Xie Y M, Meyers R E, Mertz C J, Liu X, O'Brien W D and Rosengart A J 2008 Improvement of *in vitro* thrombolysis employing magnetically-guided microspheres *Thromb. Res.* **121** 799–811
- Truelsen T, Begg S and Mathers C 2001 *The Global Burden Of Cerebrovascular Disease* (Geneva: World Health Organisation) ([www.who.int/healthinfo/statistics/bod\\_cerebrovascular\\_disease\\_stroke.pdf](http://www.who.int/healthinfo/statistics/bod_cerebrovascular_disease_stroke.pdf))
- Tyn M T and Gusek T W 1990 Prediction of diffusion-coefficients of proteins *Biotechnol. Bioeng.* **35** 327–38
- Verhaagen B, Boutsoukis C, Sleutel C P, Kastrinakis E, van der Sluis L W M and Versluis M 2014 Irrigant transport into dental microchannels *Microfluid. Nanofluid.* **16** 1165–77
- Young M E, Carroad P A and Bell R L 1980 Estimation of diffusion-coefficients of proteins *Biotechnol. Bioeng.* **22** 947–55
- Zhang J, Yan S, Yuan D, Alici G, Nguyen N T, Ebrahimi Warkiani M and Li W 2016 Fundamentals and applications of inertial microfluidics: a review *Lab Chip* **16** 10–34